International Journal of Thermal Sciences 172 (2022) 107269

Contents lists available at ScienceDirect

International Journal of Thermal Sciences

journal homepage: www.elsevier.com/locate/ijts

# Numerical investigation of a novel multistage swirl cooling conception in blade leading edge of gas turbine

Ran Yao [a], Hang Su [b], Yun Cheng [b], Jianhua Wang [a,*], Jian Pu [a,**]

[a] CAS Key Laboratory of Mechanical Behavior and Design of Materials, Department of Thermal Science and Energy Engineering, University of Science and Technology of China, Jinzhai Road No. 96, Hefei, 230027, Anhui, PR China
[b] Research Institute of Aero-engine Corporation of China, Shenyang, Liaoning, PR China

ARTICLE INFO

*Keywords:*
Multistage swirl cooling
Heat transfer enhancement
Conjugate heat transfer
Leading edge of turbine blade

ABSTRACT

Swirl cooling is one of the latest and promising internal cooling strategies, which has been widely reported in the designs of the turbine blade leading edges. Based on the traditional single-stage swirl cooling configuration, this paper introduces a novel conception of multistage swirl cooling configuration (two and three stage), aiming to improve the cooling performances of the leading edges without increasing the cooling air consumption. In the new multistage configurations, the vortex chamber is divided into several stages, so that the tangential velocity of cooling air is significantly increased. To reveal the heat transfer and flow characteristics of cooling air in the multistage swirl cooling configuration, a series of numerical simulations are conducted by conjugate heat transfer algorithm under the realistic conditions of gas turbine operations and the real leading edge model of a VKI turbine blade. The numerical results indicate that: under the same coolant mass flow rate, the averaged Nusselt number in the three-stage swirl cooling structure is at least over 75% higher than that in the single-stage structure, and the Nusselt number distribution is also more uniform. At $Re_D = 40{,}000$, the surface temperature averaged over the entire leading edge wall of the three-stage swirl cooling structure can be nearly 100 K lower than that in the single-stage one. The significant heat transfer enhancement of multistage swirl cooling is at the cost of a higher total pressure loss. However, if the bends connecting the adjacent stages are modified into round-shaped, the pressure loss can be significantly decreased, therefore the thermal performances of the multistage swirl cooling models are higher than that of the single-stage model.

## 1. Introduction

In order to get a higher thermal efficiency or power output, modern gas turbines are usually operating at the high temperatures exceeding the melting point of turbine blade materials. Therefore, it is necessary to develop effective cooling methods, especially for the leading edge of turbine blades, because the leading edge bears heavy heat load and aerodynamic force [1].

The swirl cooling (also called vortex cooling) scheme is one of the promising internal cooling strategies [2] in the blade leading edge applications. Early in 1959, Kreith and Margolis [3] firstly found that in a cylindrical pipe, the heat transfer coefficient is significantly enhanced by swirling flow. Then, Glezer et al. [4,5] started to apply the swirling chamber to real blade leading edge. In their experiments, the swirling flow was introduced by discrete tangential slots, and the surface heat transfer coefficients were measured by an IR radiometer. Later, Ligrani et al. [6] and Hedlund & Ligrani [7] investigated the heat transfer and flow phenomena in different vortex chambers, and found that the arrays of Görtler vortices along the chamber surface had a positive effect to increase local heat transfer. In their another work, Ligrani et al. [8] compared the heat transfer coefficients of different internal cooling strategies of a turbine blade leading edge, and found that the swirl cooling structure provided the highest levels of heat transfer augmentation. Using transient liquid crystal technique, Ling et al. [9] compared the local heat transfer coefficients between a swirl cooling system and a normal impingement cooling system, and claimed that the swirl cooling system could provide a more uniform heat transfer distribution in axial direction.

In recent years, there have been a large number of experimental and numerical investigations focused on the complicated turbulent flow and heat transfer characteristics inside the vortex chambers of swirl cooling.

* Corresponding author.
** Corresponding author.
*E-mail addresses:* jhwang@ustc.edu.cn (J. Wang), jianpu@ustc.edu.cn (J. Pu).

https://doi.org/10.1016/j.ijthermalsci.2021.107269
Received 23 April 2021; Received in revised form 12 July 2021; Accepted 3 September 2021
Available online 16 September 2021

**Nomenclature**

| | |
|---|---|
| $x, y, z$ | Coordinates, mm |
| N | Stage number |
| $C$ | Chord length, mm |
| $P$ | Pitch length, mm |
| $H$ | Blade height, mm |
| $D_L$ | Diameter of blade leading edge, mm |
| $\alpha_1$ | Inlet angle, |
| $\alpha_2$ | Outlet angle, |
| $L$ | Length of coolant chamber, mm |
| $W$ | Width of coolant chamber, mm |
| $l$ | Length of nozzle, mm |
| $w$ | Width of nozzle, mm |
| $D$ | Diameter of vortex chamber, mm |
| $\theta$ | Angle of tangential direction, |
| $h$ | Length of stage-entrance part, mm |
| $e$ | Length of conjunction section, mm |
| $T$ | Temperature, K |
| Re | Reynolds number |
| $m$ | Mass flow rate, kg/s |
| $Tu$ | Turbulent intensity |
| $\rho$ | Density, kg/m$^3$ |
| $C_p$ | Specific heat capacity, J/(kg·K) |
| $\lambda$ | Thermal conductivity, W/(m·K) |
| $h$ | Heat transfer coefficient, W/(m$^2$·K) |
| $Nu$ | Nusselt number |
| $u$ | Velocity, m/s |
| $\eta$ | Thermal performance |
| $q$ | Heat flux, W/m$^2$ |
| $\Phi$ | Overall cooling effectiveness |
| $C_{Pt}$ | Total pressure coefficient |
| $P_t$ | Total pressure, Pa |

*Acronyms*

| | |
|---|---|
| MSC | Multistage swirl cooling |
| VKI | von Karman Institute |
| MFR | Mass flow ratio |
| TR | Temperature ratio |
| CV | Corner vortex |
| RANS | Reynolds-averaged Navier- Stokes |

*Subscripts*

| | |
|---|---|
| $c$ | Coolant |
| $\infty$ | Mainstream |
| $D$ | Diameter of vortex chamber |
| $iw$ | Inner wall |
| $ow$ | Outer wall |
| $ref$ | reference |
| $f$ | fluid |
| $in$ | Stage inlet |
| $exit$ | Exit of vortex chamber |
| $1, 2, 3$ | Stage number |
| $j$ | Coolant jet |

Through both experimental and numerical methods, Biegger et al. [10] investigated the fluid flow and heat transfer mechanism of swirl cooling in a swirl tube. They observed the double helix vortex structure inside the swirl tube, which led to a high circumferential velocity and a high heat transfer rate. Rao et al. [11] compared the heat transfer and pressure loss in two swirl tubes between one and five tangential nozzles, and concluded that at the same mass flow rate, the swirl tube with five nozzles showed a more uniform heat transfer distribution and a less total pressure loss. Using Ling et al. [9]'s experimental model, Liu et al. [12,13] numerically studied the effects of coolant Reynolds number, nozzle aspect ratio and injection angle on the heat transfer and pressure loss characteristics. By numerical simulations, Du et al. [14–16] systematically investigated the influences of the geometrical parameters of nozzle, aerodynamic parameters and rotational conditions on flow and heat transfer behaviors. Fan et al. [17,18] used a semi-cylindrical shaped vortex chamber to match turbine blade leading edges, and numerically compared various internal cooling methods of a real blade leading edge. They claimed that the swirl cooling structure can reach the highest heat transfer enhancement, the most uniform Nusselt number distribution and the largest thermal performance factor.

To further improve the utilization efficiency of cooling air, considering the design requirement of blade leading edge, a novel conception called "multistage swirl cooling" (MSC) is suggested in this work. The similar idea of multistage cooling was reported by Liu and Zhang [19,20], but their multistage cooling means a series of impingement cooling, and the target wall is a flat plate without swirling cooling air. In our new MSC configuration, the whole vortex chamber is divided into two or three stages. After passing through the first stage with highly-increased tangential velocity, the cooling air can be re-used in the later stages, therefore the cooling performance is improved without increasing the cooling air consumption.

In addition, in the previous investigations of swirl cooling, the simplified boundary conditions, such as isothermal or constant heat flux boundaries, were widely used to substitute the real conjugate heat transfer conditions. Although the conclusions drawn by the simplified boundary conditions can provide useful information, the real cooling information on the leading edge wall is still missing. Wang et al. [21] reported that the differences between the numerical results obtained by simplified and realistic boundary conditions are quite noticeable. In this work, by a series of validated conjugate heat transfer numerical simulations, the heat transfer and flow characteristics of single-stage and multistage swirl cooling structures are studied by the real leading edge model of a VKI blade and under the real operation conditions. The aim of this work is to provide the internal cooling researchers and designers of turbine blade a new selection of enhancing heat transfer performances.

## 2. Geometrical models of the single-stage and multistage swirl cooling

The swirl cooling structure used in this work is planted in the real leading edge of a VKI turbine blade with linear cascade reported by Arts [22]. The chord length of the VKI blade ($C$) is 80 mm, the pitch of the blade ($P$) is 53.6 mm, the height of the blade ($H$) is 100 mm, and the diameter of the blade leading edge ($D_L$) is 6.25 mm. The other detailed parameters of the blade are given in Table 1 and Fig. 1(a–b).

As Fig. 1 shows, the conventional single-stage swirl cooling model consists of a cuboid coolant chamber, a cylindrical vortex chamber and six tangential nozzles. Coolant firstly enters into the coolant chamber, then ejects from the six tangential nozzles to the vortex chamber. The length ($L$) and width (W) of the vortex chamber are 5 mm and 3 mm,

**Table 1**
Geometrical parameters of the VKI blade and cascade.

| Parameters | Value |
|---|---|
| Pitch length, $P$ | 53.6 mm |
| Chord length, $C$ | 80 mm |
| Inlet angle, $\alpha_1$ | 30° |
| Outlet angle, $\alpha_2$ | 38.5° |
| Diameter of leading edge, $D_L$ | 6.25 mm |
| Blade height, $H$ | 100 mm |

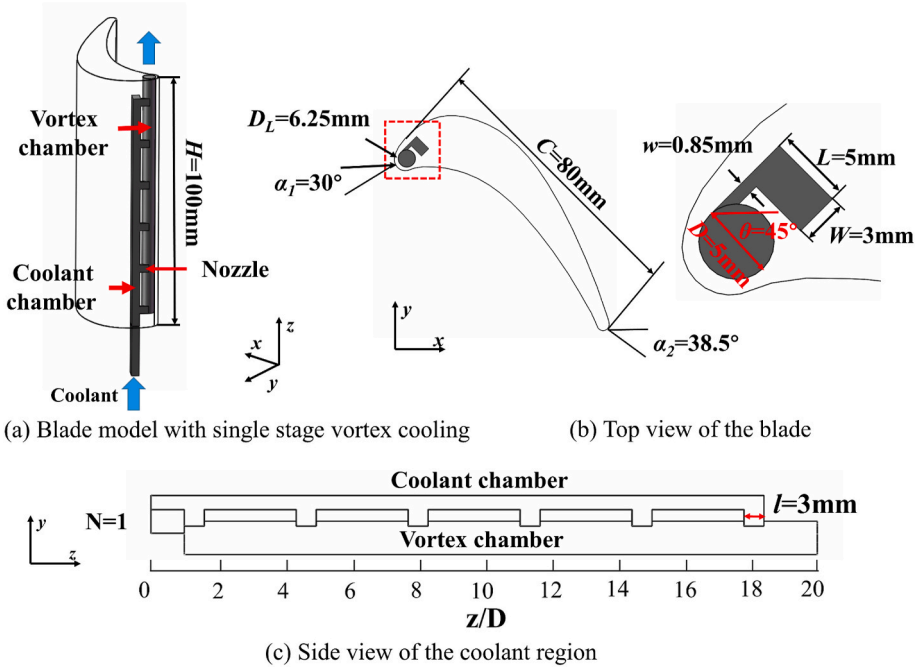


(a) Blade model with single stage vortex cooling (b) Top view of the blade

(c) Side view of the coolant region

**Fig. 1.** Single-stage swirl cooling structure in the blade leading edge.

respectively, while the dimensions of the nozzles ($l \times w$) are 3 mm × 0.85 mm. The diameter of the vortex chamber is 5 mm, and the angle between the tangential direction and $x$ axis is 45°. The locations of the six nozzle centers are shown in Fig. 1 (c) and Table 2.

Fig. 2 shows the MSC models with two and three stages (N = 2 and N = 3), respectively. In the models, the parameters of the coolant chamber, vortex chamber and six nozzles are the same to the single-stage model (N = 1). However, the vortex chamber is divided into two or three stages, and each stage contains the same number (three or two) of nozzles. As shown in Fig. 2 (a), instead of simultaneously ejecting from all the six nozzles, the coolant firstly passes through the three or two nozzles in the first stage, and then enters into the subsequent stage. As Fig. 2 (b) shows, the length of the stage-entrance part ($h$) and the conjunction section between two adjacent stages (e) is 3 mm and 1 mm, respectively.

## 3. Numerical methodology

### 3.1. Governing equations and boundary conditions

Steady-state three-dimensional numerical simulations of the single-stage and multistage swirl cooling configurations were conducted. The SST $k$–$\omega$ turbulence model was used to enclose the governing equations as follows:

**Table 2**
Location of the six nozzle centers.

| Nozzle | 1 | 2 | 3 | 4 | 5 | 6 |
|---|---|---|---|---|---|---|
| Location (z/D) | 1.30 | 4.66 | 8.02 | 11.38 | 14.74 | 18.10 |

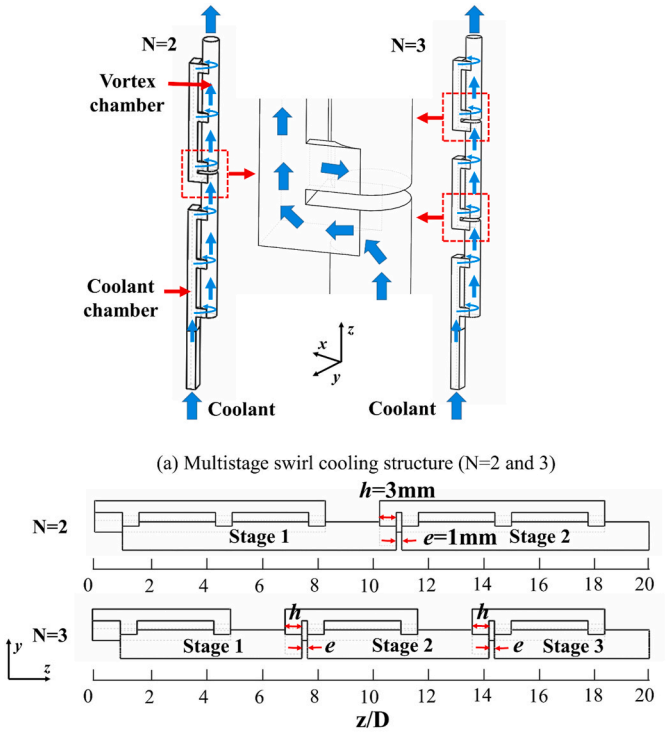


(a) Multistage swirl cooling structure (N=2 and 3)

(b) Side view of the coolant region

**Fig. 2.** Multistage swirl cooling configurations (N = 2 and N = 3).

Mass conservation:

$$\nabla \cdot (\rho \vec{u}) = 0 \tag{1}$$

Momentum conservation:

$$\nabla \cdot (\rho \vec{u}\vec{u}) = -\nabla P + \nabla \cdot (\bar{\bar{\tau}}) \tag{2}$$

Energy conservation:

$$\nabla \cdot (\vec{u}(\rho E + P)) = \nabla \cdot \left( k_{eff} \nabla T + \left( \bar{\bar{\tau}}_{eff} \cdot \vec{u} \right) \right) \tag{3}$$

where:

$$\bar{\bar{\tau}} = \mu \left( (\nabla \vec{u} + \nabla \vec{u}^T) - \frac{2}{3} \nabla \cdot \vec{u} I \right) \tag{4}$$

$$E = h - \frac{P}{\rho} + \frac{u^2}{2} \tag{5}$$

Transport equations for the SST $k$-$\omega$ model:

$$\frac{\partial}{\partial x_i}(\rho k u_i) = \frac{\partial}{\partial x_j}\left( \Gamma_k \frac{\partial k}{\partial x_j} \right) + G_k - Y_k \tag{6}$$

$$\frac{\partial}{\partial x_i}(\rho \omega u_i) = \frac{\partial}{\partial x_j}\left( \Gamma_\omega \frac{\partial \omega}{\partial x_j} \right) + G_\omega - Y_\omega + D_\omega \tag{7}$$

The definitions of each term in the SST $k$-$\omega$ turbulence model are exhibited in ANSYS Fluent documents [23].

To reduce the amount of calculation, the periodic condition is used, and the entire computational domain consists of three regions: the mainstream region, the solid region, and the coolant region, as shown in Fig. 3. To mitigate the influences of the mainstream inlet and outlet on the numerical results, the mainstream region is extended 1.0 time of chord length ($C$) upstream from the leading edge of the blade, and 1.5 $C$ downstream from the trailing edge, respectively.

The boundary conditions in the swirl cooling configuration are illustrated in Fig. 3. In both lateral sides of the mainstream region, translational periodic boundary condition is used. All interfaces of fluid and solid regions are set as coupled walls, which means that the heat flux can pass through the fluid-solid interface, but the mass flow is not allowed to pass through the interface. The walls on the upside and downside are set as adiabatic walls. At both inlets of mainstream and coolant, the mass flow rates, temperatures and turbulence intensities are given. The outlets of mainstream and coolant are set as pressure outlet, where the static pressures are given.

The detailed parameters at the two inlets are listed in Table 3. The temperatures of mainstream and coolant inlets are 1500 K and 600 K, respectively, which corresponds to a real large temperature ratio (TR) of 2.5. In the mainstream inlet, the Reynolds number based on the chord length is $1.75 \times 10^5$, which is in the same level of several typical subsonic gas turbine experiments [24,25]. Three different mass flow rates are given at the coolant inlet, and the Reynolds number based on the vortex chamber diameter are 20,000, 30,000 and 40,000, respectively. The corresponding mass flow ratio (MFR) of cooling air to mainstream is respectively 0.28%, 0.42% and 0.56%. The turbulence intensities ($Tu$) at both inlets are 5%, which is a moderate value.

**Table 3**
Boundary conditions at the mainstream and coolant inlets.

| Boundary conditions | Value | | |
|---|---|---|---|
| $T_\infty$ | 1500 K | | |
| $T_c$ | 600 K | | |
| $TR$ | 2.5 | | |
| $m_\infty$ | 0.6536 kg/s | | |
| $Re_\infty$ | $1.75 \times 10^5$ | | |
| $m_c$ | $1.83 \times 10^{-3}$ kg/s | $2.75 \times 10^{-3}$ kg/s | $3.67 \times 10^{-3}$ kg/s |
| $Re_D$ | 20,000 | 30,000 | 40,000 |
| MFR | 0.28% | 0.42% | 0.56% |
| $Tu_\infty$ | 5.0% | | |
| $Tu_c$ | 5.0% | | |

### 3.2. Mesh generation and grid independence research

The meshes in the computational domain are generated using the commercial software ANSYS Fluent Meshing 15.0. As shown in Fig. 4, the mainstream and coolant regions are filled by polyhedral cells for the main body, and prismatic cells near the walls. 12 layers of prism grids are stretched from the solid walls to the fluid region, and the thickness of the first layer is carefully set to ensure the value of y+ is less than 1.0. In the solid region, only polyhedral cells are generated.

The grid independence of numerical results is validated by three groups of mesh strategies with different cell numbers, as shown in Table 4. Under the condition of $Re_D$ = 20,000, the surface averaged Nusselt numbers ($Nu$) at the vortex chamber are calculated by the three swirl cooling models using the three mesh strategies. From the results, one can find that the maximal difference between the first and second strategies is about 1%, but less than 0.5% between the second and third groups. Therefore, to save computational resource and ensure calculation accuracy, the second group of mesh strategy is selected in the following work.

### 3.3. Computational settings and convergence criterion

In the present work, the mainstream and coolant are set as ideal gas air, and the dynamic viscosity is calculated by the Sutherland law. As shown in Eqs. (8) and (9), the polynomial empirical formulas are used to

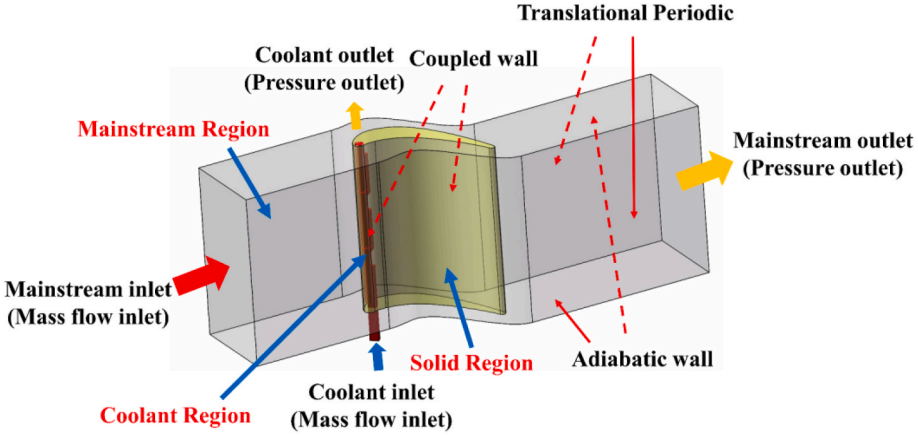


**Fig. 3.** Computational domain and boundary conditions in MSC configuration.

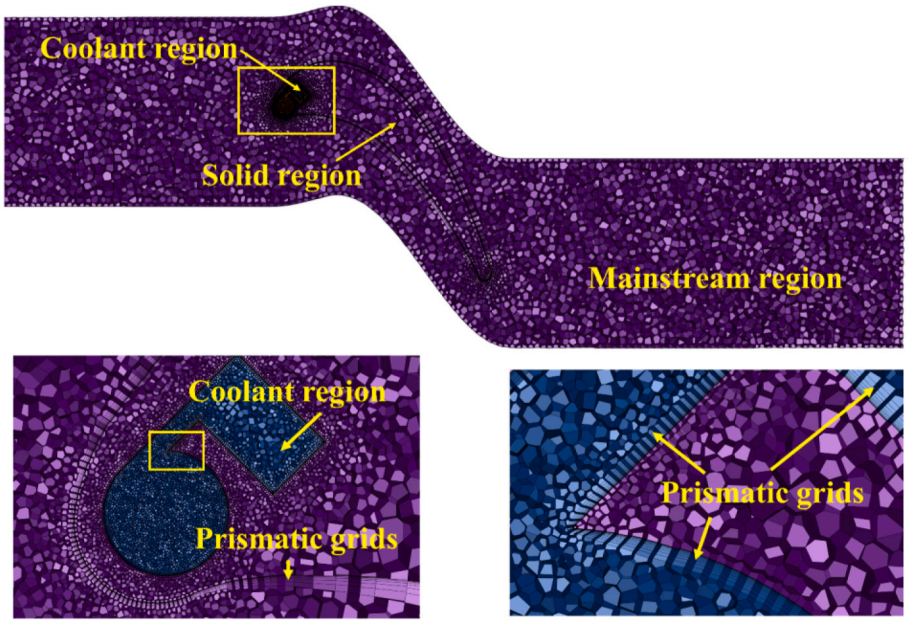


**Fig. 4.** Vol grids in the computational domain.

**Table 4**
Three groups of mesh strategies and surface averaged *Nu* at $Re_D = 20{,}000$.

| Models | Cell number | | | Surface averaged *Nu* | | |
|---|---|---|---|---|---|---|
| | Group 1 | Group 2 | Group 3 | Group 1 | Group 2 | Group 3 |
| N = 1 | 13,345,834 | 18,605,251 | 27,156,547 | 96.32 | 97.65 | 97.93 |
| N = 2 | 13,624,358 | 18,842,364 | 27,584,962 | 142.30 | 143.67 | 144.01 |
| N = 3 | 14,354,850 | 19,305,229 | 27,906,714 | 170.61 | 171.40 | 171.72 |

calculate the specific heat capacities ($C_p$) and thermal conductivities ($\lambda$) based on the Ref. [26], which is valid in the temperature range from 250 K to 1800 K. The solid blade is made of stainless steel with a constant density of 8055 kg/m$^3$. According to Ref. [27], the specific heat capacities ($C_p$) and thermal conductivities ($\lambda$) of stainless steel are functions of temperature as shown in Eqs. (10) and (11).

For air [26]:

$$C_p = 1.2665 \times 10^{-10}T^4 - 5.8145 \times 10^{-7}T^3 + 9.0458 \times 10^{-4}T^2 - 3.5186 \times 10^{-1}T + 1.0151 \times 10^3 \left(J \cdot K^{-1} \cdot kg^{-1}\right) \quad (8)$$

$$\lambda = 1.3228 \times 10^{-11}T^3 - 4.6304 \times 10^{-8}T^2 + 1.0241 \times 10^{-4}T - 9.3851 \times 10^{-4} \left(W \cdot m^{-1} \cdot K^{-1}\right) \quad (9)$$

For solid [27]:

$$C_p = 472 + 13.6 \times 10^{-2}T - 2.82 \times 10^6 T^{-2} \left(J \cdot K^{-1} \cdot kg^{-1}\right) \quad (10)$$

$$\lambda = 9.2 + 0.0175T - 2 \times 10^6 T^{-2} \left(W \cdot m^{-1} \cdot K\right) \quad (11)$$

In the calculation process, the SST k-ω model developed by Menter [28] is selected as the turbulence model to solve the steady state Reynolds-averaged Navier-Stokes (RANS) equations. The turbulent Prandtl number is set as 0.85. Second order upwind scheme is used to discretize the momentum, energy, and turbulence transport equations. The residual levels of continuity, velocity and turbulence variables are given as $1 \times 10^{-4}$, but $1 \times 10^{-6}$ for the energy equations. In order to ensure the solution convergence, the unbalanced mass should be less than 0.5%, and the surface averaged Nusselt number on the vortex chamber is monitored. The numerical calculations are carried out by the supercomputing system in the Supercomputing Center of University of Science and Technology of China, with eight groups of 24-core Intel (R) Xeon (R) E5-2680 v3 central processing units.

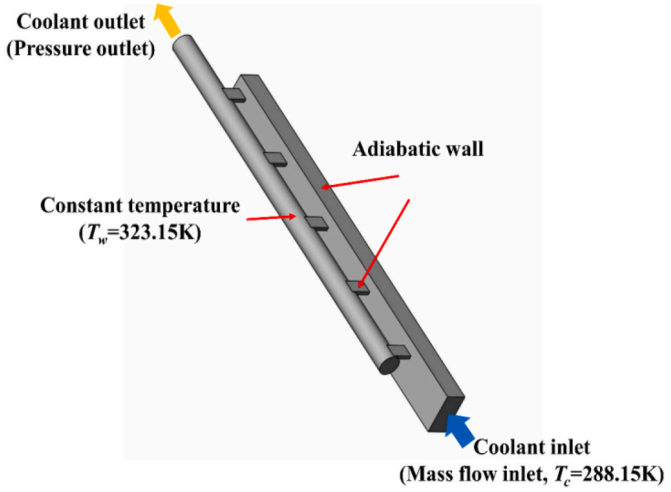


**Fig. 5.** Geometrical model and boundary conditions of reference [11] for validation.

### 3.4. Validation of the turbulence model and numerical method

As MSC is a novel conception, there is no similar experiment in the current published references, therefore in the validation of our numerical method, the experimental data of single-stage swirl cooling reported by Rao et al. [11] are used. The validation of the numerical method is

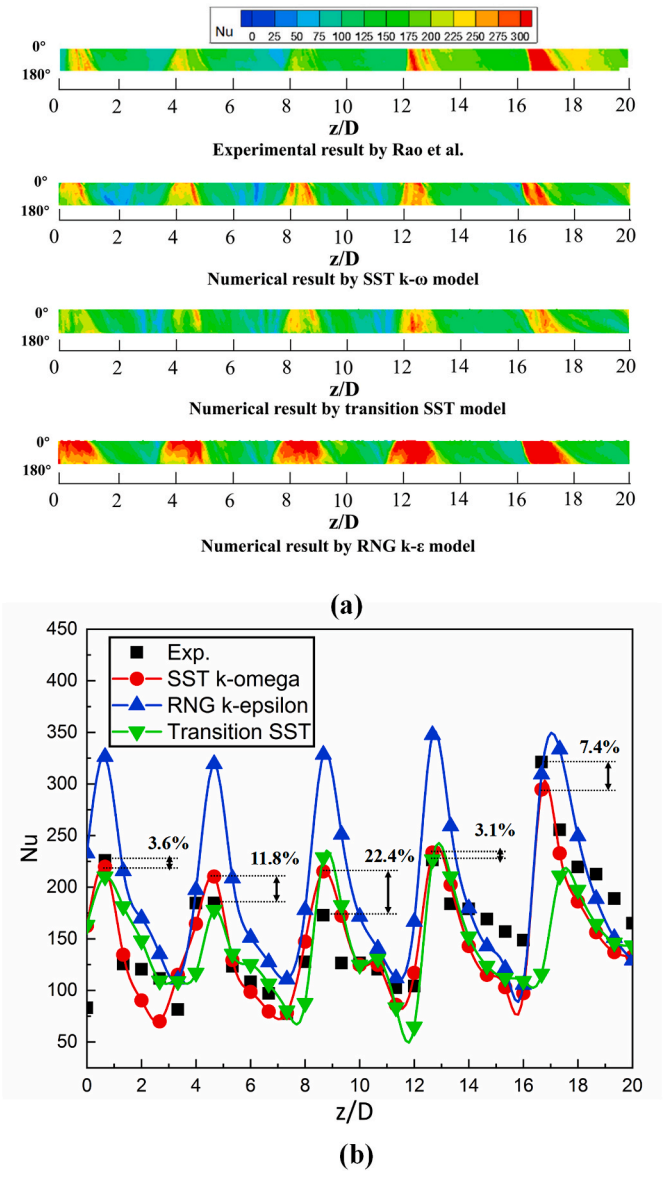


**Fig. 6.** Comparison of simulation and experiment (a) Local *Nu*; (b) Averaged *Nu*.

conducted using the experimental condition and swirl cooling model as shown in Fig. 5. Three turbulence models are selected for comparison, including RNG k-ε, SST k-ω and transition SST model.

At coolant $Re_D$ = 40,000, Fig. 6 (a) and (b) compare the local and circumferential averaged Nusselt number (*Nu*) with the experimental data of reference [11]. From the comparison, one can find the same trend of *Nu* distributions. However, the Nusselt number predicted by RNG k-ε model is significantly higher than the experimental data; predicted by the transition SST model is obviously underestimated in the region of 16 < z/D < 20; and predicted by SST k-ω turbulence model illustrates a good agreement with the experimental data. Therefore, SST k-ω turbulence model is selected in the following simulations.

## 4. Results and discussions

Using the validated numerical method and mesh strategy, numerical simulations are conducted under the three mass flow ratios (0.28%, 0.42% and 0.56%) using the three swirl cooling configurations: (N = 1, 2 and 3), respectively.

### 4.1. Local heat transfer rate

To investigate the heat transfer characteristics on the vortex chamber, local heat transfer coefficient and Nusselt number (*Nu*) are defined by:

$$h = \frac{q}{T_{iw} - T_{ref}} \tag{12}$$

$$Nu = \frac{hD}{\lambda_f}. \tag{13}$$

where $q$ and $\lambda_f$ are the heat flux on the vortex chamber surface and the local fluid thermal conductivity, $D$ is the diameter of the vortex chamber, $T_{iw}$ and $T_{ref}$ represent the local temperature on the vortex chamber inner wall, and the fluid bulk temperature, respectively.

Fig. 7 shows *Nu* distributions obtained by three cases (N = 1, 2 and 3) at $Re_D$ = 20,000. When N = 1, one can find the following phenomena: 1) *Nu* achieves the peak values near each nozzle. This phenomenon is reasonable, because the coolant passing through the nozzles directly impinges the chamber wall with high tangential velocity. 2) Along the axial flow direction, the averaged *Nu* in the downstream region (15 < z/D < 20) is generally higher. Rao et al. [11] also discovered this phenomenon and explained it by using non-uniform coolant allocation in each nozzle. 3) In the circumferential direction, the high *Nu* region gradually extends from each nozzle exit to downstream, i.e. from 0° to 180°. In this process, the maximal value of *Nu* decreases.

When N = 2 and N = 3, the local heat transfer characteristics show noticeable differences from N = 1. At first, *Nu* is much larger than that of N = 1, in general. This is caused by the much larger tangential velocity of the coolant impingement, which is approximately as twice or three times large as that of N = 1, respectively. Secondly, the distributions of *Nu* in N = 2 and 3 cases become more uniform, and the areas with low *Nu* between two adjacent nozzles in the single-stage configuration almost disappear.

### 4.2. Averaged Nu distributions at different $Re_D$s

Fig. 8(a–c) exhibit the circumferential averaged *Nu* distributions obtained at $Re_D$ = 20,000, 30,000 and 40,000, respectively. From Fig. 8, one can find the following phenomena: 1) The averaged *Nu* increases distinctly with $Re_D$ (coolant mass flow rate), and the peak values of *Nu* appear approximately at z/D = 1.3, 4.7, 8.0, 11.4, 14.7 and 18.1, which corresponds to the six exits of the nozzles. 2) The valley values of *Nu*

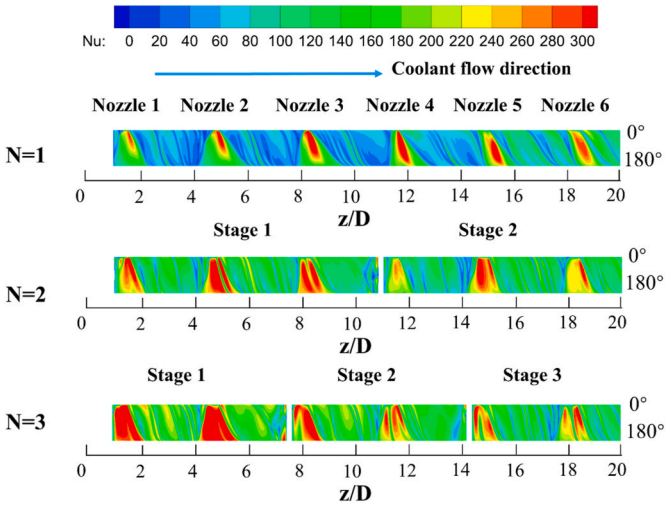


**Fig. 7.** Nusselt number distributions on the vortex chamber wall at $Re_D$ = 20,000. (For interpretation of the references to colour in this figure legend, the reader is referred to the Web version of this article.)

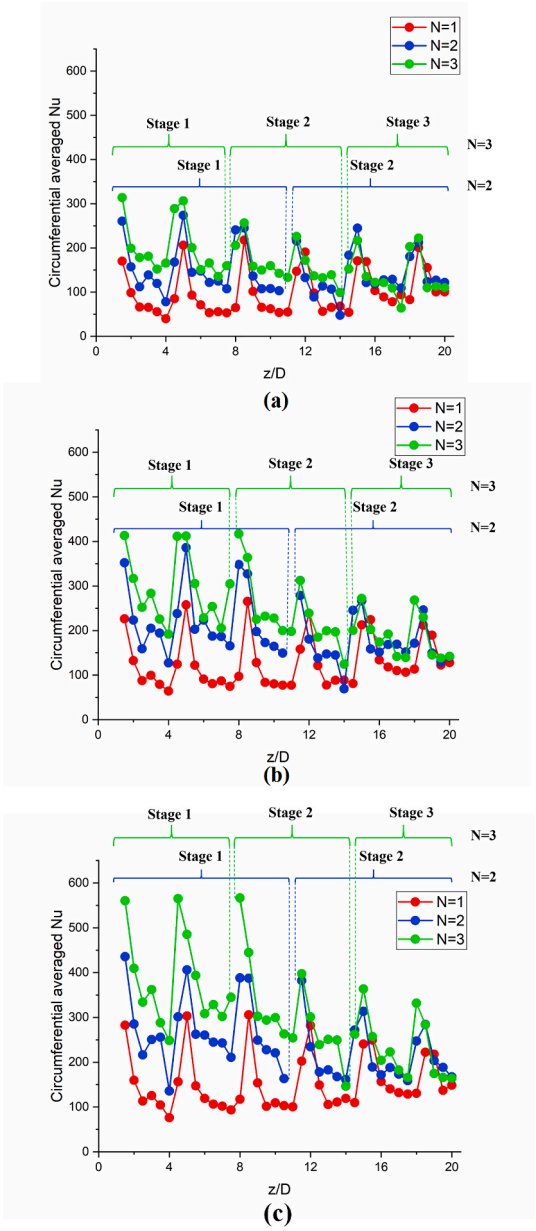


**Fig. 8.** Circumferential averaged *Nu* at (a)$Re_D$ = 20,000, (b)$Re_D$ = 30,000 and (c)$Re_D$ = 40,000. (For interpretation of the references to colour in this figure legend, the reader is referred to the Web version of this article.)

always appear between the two adjacent nozzles. 3) When N = 1, the peak value near the nozzle can be as 5 times large as its neighboring valley value. But with an increase of N, the ratio of the peak value to the neighboring valley value decreases, which indicates that *Nu* distribution is more even. 4) In the downstream region of 16 < z/D < 20, at the same $Re_D$, the influence of the stage number N on the averaged *Nu* is not significant.

The global area-averaged *Nu* over the vortex chamber wall at three coolant Reynolds numbers are calculated, and the numerical results are also compared with the previous single-stage swirl cooling data of Rao et al. [11] and Fan et al. [17]. As a reference, $Nu_0$ calculated by Sieder & Tate's correlation for axial flow in a cylindrical pipe considering the varying thermal property [29] is also included:

$$Nu_0 = 0.024 Re_D^{4/5} Pr^{1/3} \left(\frac{\mu_{ref}}{\mu_\infty}\right)^{0.14} \quad (14)$$

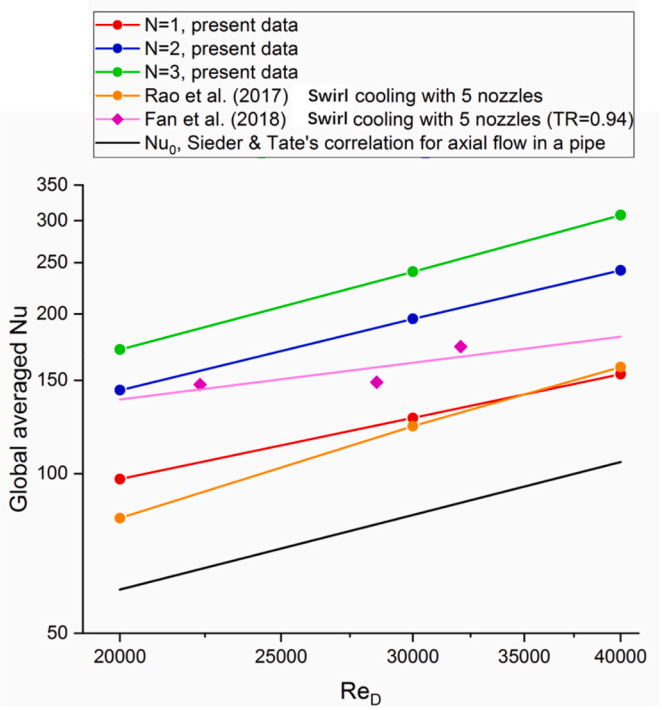


**Fig. 9.** Comparison of averaged *Nu* between different cooling structures.

Fig. 9 exhibits the heat transfer performances between the different cooling structures. It is clear that, all the averaged Nusselt numbers of swirl cooling structures are significantly higher than $Nu_0$ obtained by the case of a cylindrical pipe (axial flow) [29]. The present *Nu* data of N = 1 is very close to the experimental data of reference [11], but a little lower than that by Fan et al. [17]'s work with five nozzles at a temperature ratio of 0.94.

From the data of *Nu*, one can also find that the values of global averaged *Nu* obtained by the present multistage swirl cooling configurations are obviously higher than all the single-stage data, which indicates that the increase of N can significantly increase the global *Nu*. At each $Re_D$, the increase of global averaged *Nu* from N = 1 to N = 2 is over 45%, and about 20% from N = 2 to N = 3. Comparing the cases between N = 1 and N = 3, the global *Nu* is increased by 75.5% at $Re_D$ = 20,000, 88.7% at $Re_D$ = 30,000, and 99.5% at $Re_D$ = 40,000.

### 4.3. Cooling effectiveness on the target wall at blade leading edge

The overall cooling effectiveness (Φ) is defined by dimensionless temperature on the target wall as follows:

$$\Phi = \frac{T_\infty - T_{ow}}{T_\infty - T_c}, \quad (15)$$

where $T_\infty$, $T_c$ and $T_{ow}$ are the temperatures at the inlets of mainstream and coolant, outside wall of the blade leading edge, respectively.

Fig. 10 shows the local overall cooling effectiveness obtained in the cases of N = 1, 2 and 3 at $Re_D$ = 20,000. From Fig. 10, one can find the following two important phenomena: 1) When N = 2 and 3, the target surfaces can obtain higher overall cooling effectiveness, but the values of Φ generally decreases along the axial flow direction. This phenomenon is reasonable, because the temperature of coolant rises along the axial flow, as listed in Table 5. Although coolant enters the inlet at the same temperature of 600 K, the final exit temperature ($T_{exit}$) increases, and the increasing amplitude rises with the stage number N. This phenomenon implies that the total usage efficiency of coolant rises with the final exit temperature. 2) When N = 2 and 3, there are small conjunction sections (1 mm length) between two adjacent stages, i.e., 10.88 < z/D < 11.08 in

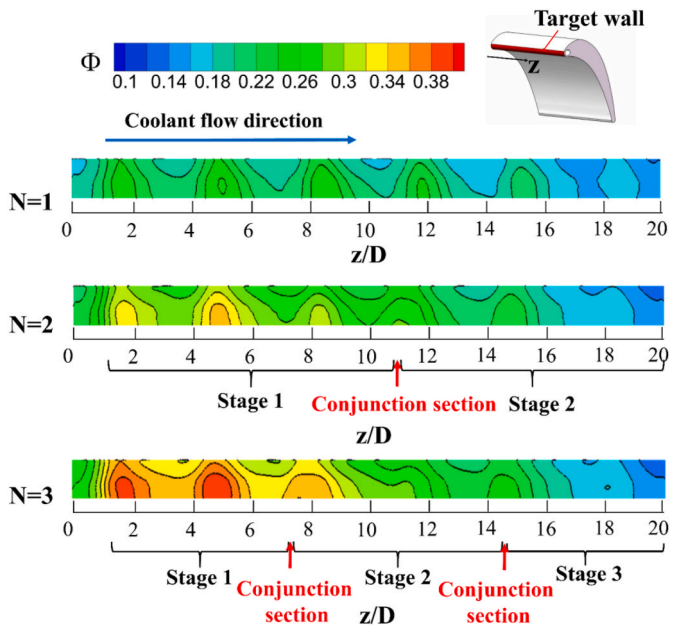


**Fig. 10.** Overall cooling effectiveness on the target wall at $Re_D = 20{,}000$. (For interpretation of the references to colour in this figure legend, the reader is referred to the Web version of this article.)

**Table 5**
Averaged temperatures at each stage inlet and exit at $Re_D = 20{,}000$.

| | $T_{in,1}$ (K) | $T_{in,2}$ (K) | $T_{in,3}$ (K) | $T_{exit}$ (K) |
|---|---|---|---|---|
| N = 1 | 600.0 | – | – | 1039.1 |
| N = 2 | 600.0 | 949.7 | – | 1109.1 |
| N = 3 | 600.0 | 904.1 | 1093.8 | 1136.0 |

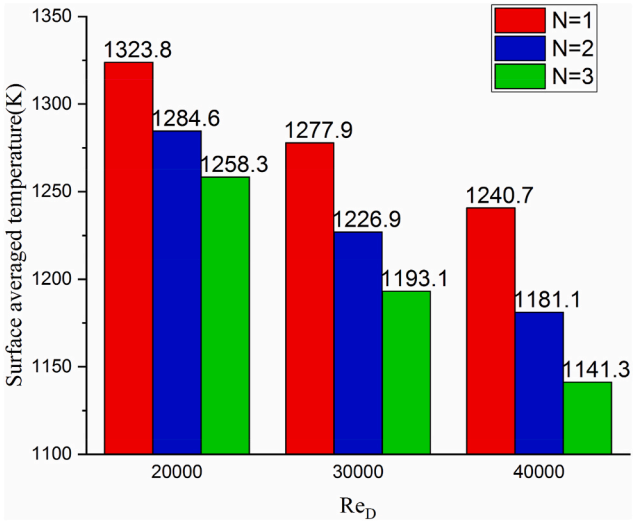


**Fig. 11.** Averaged temperature on the leading edge surface at different $Re_D$s.

N = 2 case, 7.52 < z/D < 7.72 and 14.24 < z/D < 14.44 in N = 3 case, where coolant is not directly contacted with the target wall. However, through heat conduction effect, the overall cooling effectiveness in the sections is not obviously lower compared to the neighboring regions in Fig. 10.

Fig. 11 shows the temperature averaged over the entire leading edge surface at three coolant Reynolds numbers. It is clear that an increase in $Re_D$ corresponds to an averaged temperature falling. At $Re_D = 20{,}000$, 30,000 and 40,000, the temperature drops from N = 1 to N = 3 are 65.5 K, 84.8 K and 99.4 K, respectively. This trend implies that the temperature drops increase with $Re_D$.

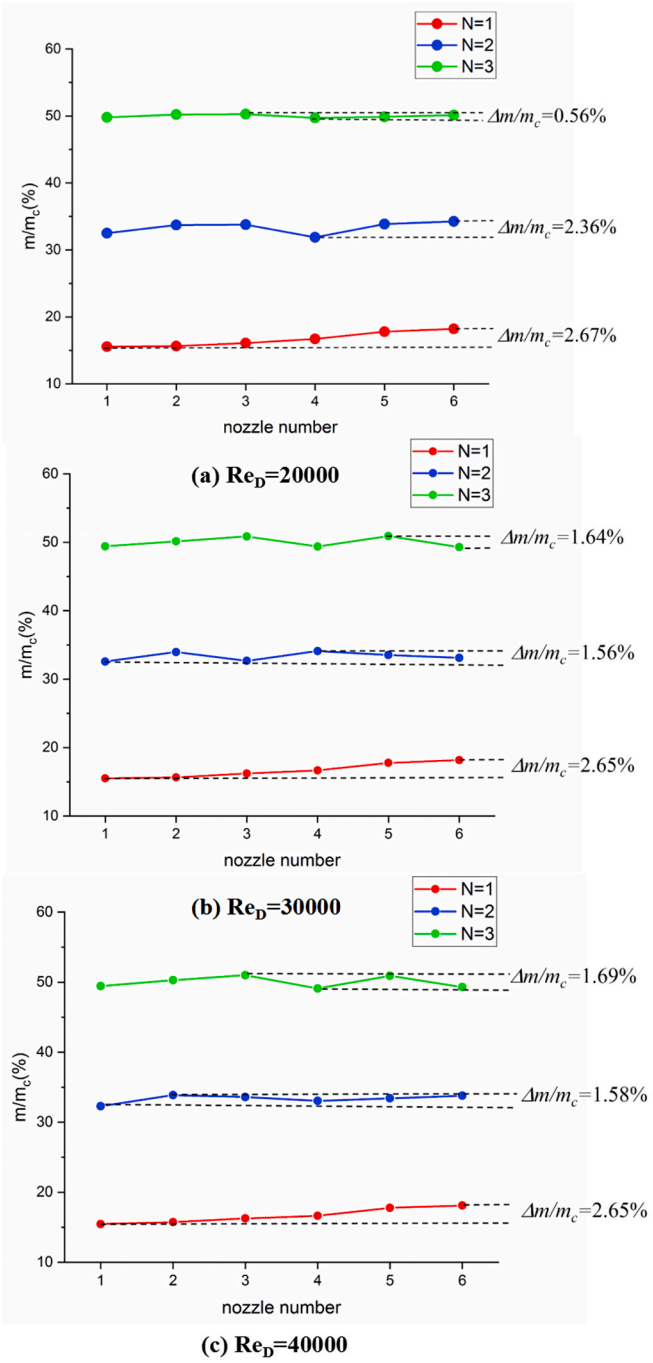


**Fig. 12.** Coolant mass flow rate allocation at 6 nozzles at different $Re_D$s.

### 4.4. Coolant allocations at each nozzle

The mass flow ratio of each nozzle to the total flow rate ($m/m_c$) is calculated at three different $Re_D$s, and Fig. 12 shows the numerical results. When N = 1, the mass flow ratio increases along the axial flow direction at all $Re_D$s, and this phenomenon was also reported in the references of [11,18,19]. The absolute difference of $m/m_c$ between the first and last nozzles is larger than 2.65%, which implies a relative difference over 17% (2.65%/15.52% at $Re_D = 30{,}000$). When N = 2, the ratio through each nozzle is almost doubled, but the maximal difference

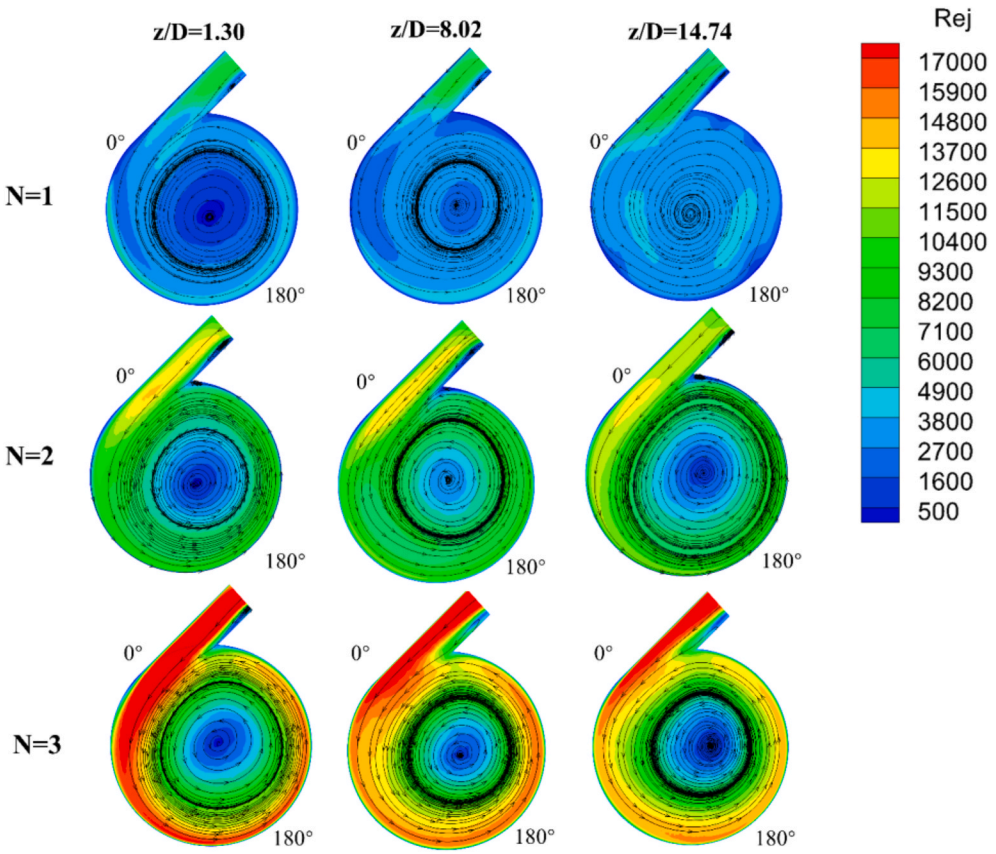


**Fig. 13.** Coolant jet Reynolds number distributions with streamlines on different *x-y* cut planes across nozzles 1, 3 and 5 at $Re_D = 20{,}000$. (For interpretation of the references to colour in this figure legend, the reader is referred to the Web version of this article.)

of the coolant allocation ($m/m_c$) decreases noticeably. When N = 3, the ratio further increases to approximate three times of N = 1, but the maximal difference of the coolant allocation is also significantly lower than that in the single-stage cases. This phenomenon implies a more uniform allocation of coolant in each nozzle, when MSC configurations are used.

### 4.5. Flow characteristics inside the vortex chamber

At $Re_D = 20{,}000$, the jet (nozzle) Reynolds number ($Re_j$) is calculated based on the hydraulic diameter of the nozzle, and Fig. 13 exhibits $Re_j$ distributions with streamlines in three *x-y* cross sections of z/D = 1.30, 8.02, 14.74, respectively, which correspond to the middle planes of the 1st, 3rd and 5th nozzles. From Fig. 13, it can be seen that in each plane, a large-scale spiral vortex appears inside the vortex chamber, and the vortex center is nearly at the geometrical center of the chamber. This vortex causes a large turbulence kinetic energy, and a thin thermal boundary layer near the chamber wall. Comparing the three configurations, it is clear that $Re_j$ is significantly higher in MSC configurations compared to N = 1. Along the circumferential chamber wall from 0° to 180°, one can find that in N = 3, the coolant with a high velocity can extend the furthest among the three configurations, which implies the best coolant impingement effect.

### 4.6. Total pressure loss characteristics

To study the characteristics of fluid friction, the total pressure loss coefficient ($C_{Pt}$) is defined as follows:

$$C_{Pt} = \frac{P_{t,in} - P_t}{P_{t,in}}. \tag{16}$$

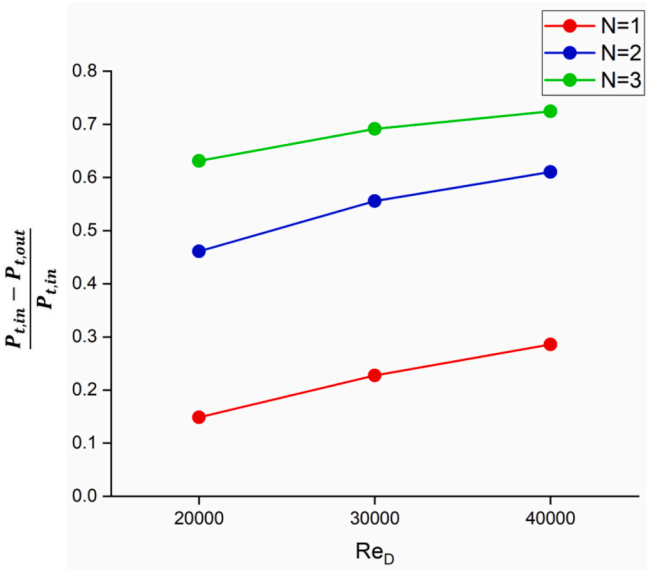


**Fig. 14.** Comparison of total pressure loss in different cooling models.

where $P_t$ is the averaged total pressure in the vortex chamber, the subscript *in* represents the coolant inlet.

Fig. 14 shows the total pressure loss from the coolant inlet to the outlet at the three Reynolds numbers. It is clear that $C_{Pt}$ increases with $Re_D$ in all cases, and at the same $Re_D$, the pressure loss coefficient increases with N. For example, at $Re_D = 40{,}000$, in N = 1 and 3 cases, $C_{Pt}$ are 0.29 and 0.72, respectively. The high pressure loss in MSC is caused

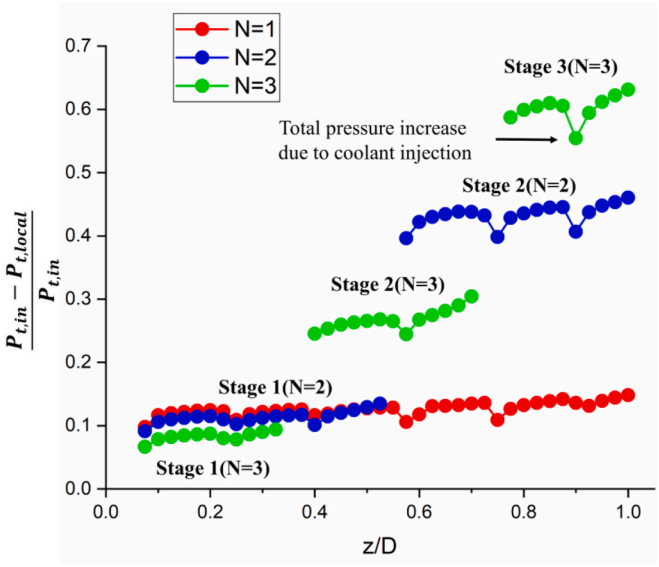


**Fig. 15.** Total pressure loss coefficient along the axial direction at $Re_D$ = 20,000. (For interpretation of the references to colour in this figure legend, the reader is referred to the Web version of this article.)

by the following two reasons: 1) The coolant impinging to the vortex chamber wall from the six nozzles contains a much higher velocity, as shown in Fig. 13. 2) The additional loss appears when the coolant passes through the two adjacent stages.

The pressure loss coefficients passing through each stage along the axial flow direction are calculated at $Re_D$ = 20,000 in the three cases N = 1, 2 and 3, and Fig. 15 quantitatively compares the numerical results. From Fig. 15, one can find that in the middle of each nozzle, there is a slight fluctuation of the coefficients due to the coolant injections from the coolant chamber. When N = 1, the pressure loss is mainly caused by the swirling flow inside the vortex chambers. When N = 2 and 3, the pressure loss between two adjacent stages jumps up significantly.

To explain the reasons of the pressure loss jump, Fig. 16(a–c) illustrate the flow characteristics on the vertical cut-planes of the three configurations. In Fig. 16(a), N = 1, the streamlines in the vortex chamber and coolant passage are almost parallel, and therefore the pressure loss coefficients are gradually increase. In Fig. 16(b–c), there

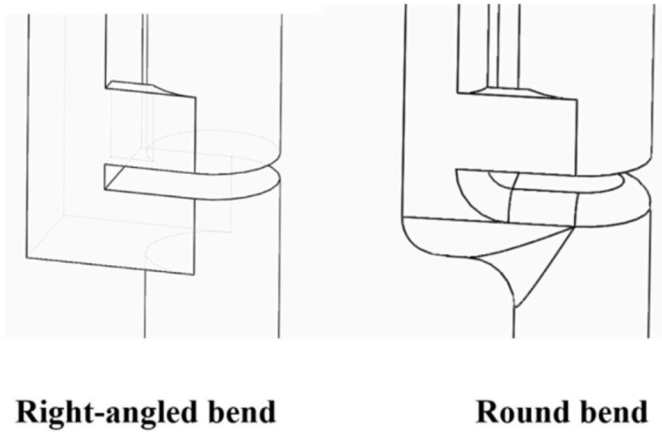


**Fig. 17.** The right-angled bend and modified round bend in MSC configurations.

are complicated vortex systems in the bend regions due to Z-shaped coolant passage, which causes very large total pressure loss.

Although MSC models can provide a significant heat transfer enhancement and more even Nusselt number distribution under the same conditions, the corresponding pressure loss coefficients are also much larger than that of single-stage swirl cooling model. To solve this problem, the right-angled bends, which connect the coolant passage and vortex chamber, are modified into round bends, as shown in Fig. 17. The corresponding fluid fields are calculated at $Re_D$ = 20,000, and the numerical results are shown in Fig. 18. It is clear that in the right-angled bend, there are two corner vortices marked by CV1 and CV2 in Fig. 18. But in the round bend, CV1 disappears, and CV2 weakens significantly.

### 4.7. Thermal performances

To estimate the comprehensive performance between the heat transfer enhancement and total pressure loss in the three swirl cooling configurations, the thermal performance ($\eta$) defined by Eq. (17) is used. In Eq. (17), $f$ is the friction factor of entire passage defined by Eq. (18), while $f_0$ is the friction factor for axial flow in a cylindrical pipe [30] for reference defined by Eq. (19):

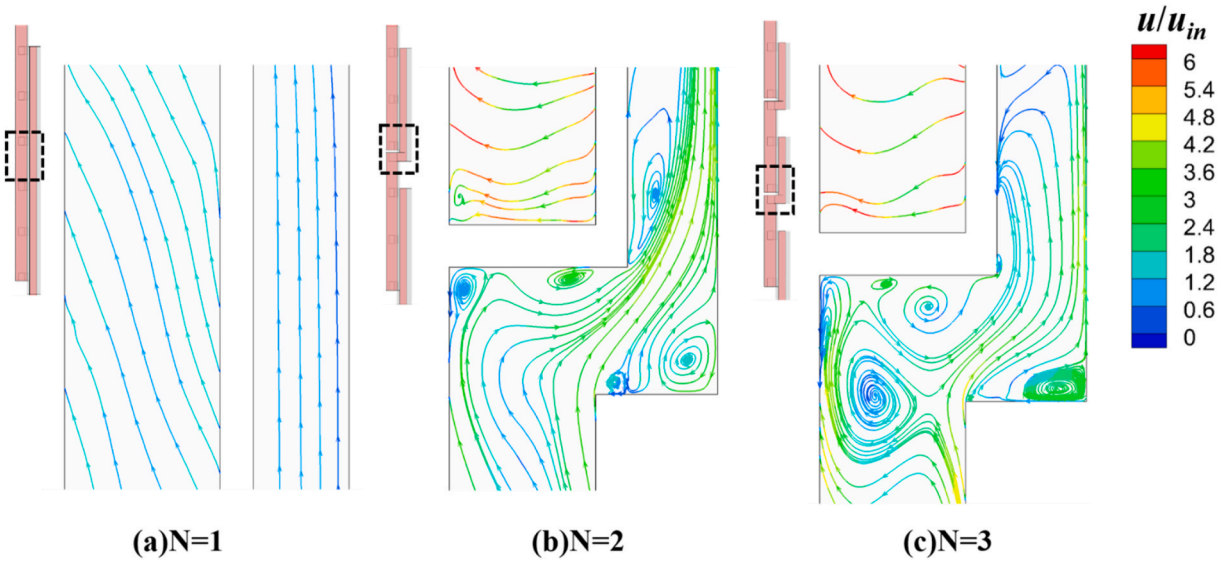


**Fig. 16.** Streamlines on the vertical cut-planes in three configurations $Re_D$ = 20,000. (For interpretation of the references to colour in this figure legend, the reader is referred to the Web version of this article.)

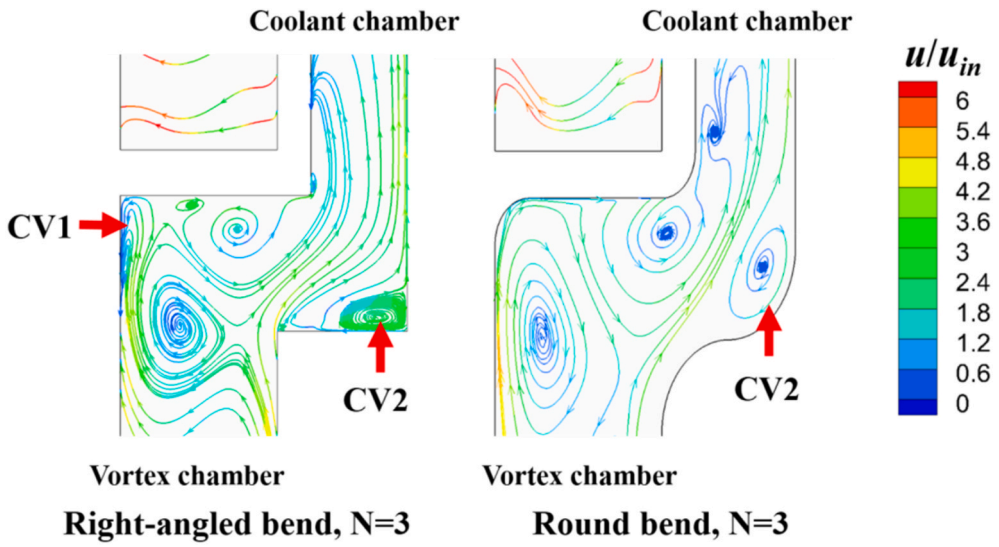


**Fig. 18.** Streamlines in the two bend regions of N = 3 at $Re_D$ = 20,000. (For interpretation of the references to colour in this figure legend, the reader is referred to the Web version of this article.)

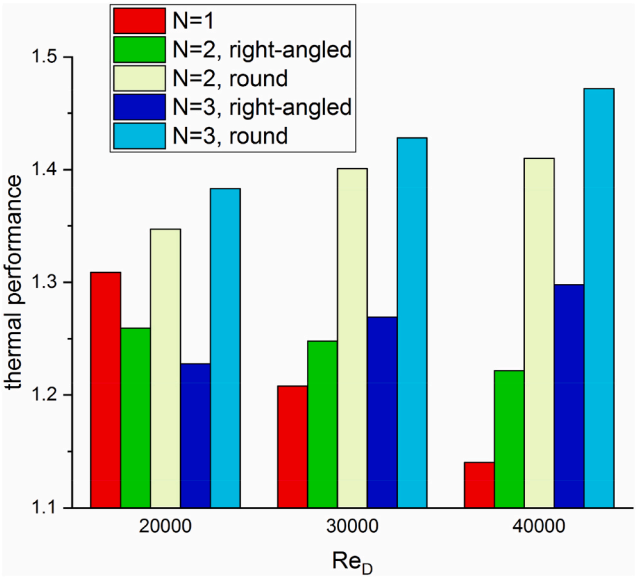


**Fig. 19.** Thermal performances in the cases N = 1, 2 and 3 with two types of bends.

$$\eta = \frac{Nu/Nu_0}{(f/f_0)^{\frac{1}{3}}} \tag{17}$$

$$f = \frac{P_{t,in} - P_{t,out}}{4\frac{H}{D}\left(\frac{1}{2}\rho_{in}\overline{u_{in}^2}\right)} \tag{18}$$

$$f_0 = (0.790\ln Re_D - 1.64)^{-2} \tag{19}$$

Fig. 19 exhibits the thermal performances ($\eta$) in the cases of N = 1, 2 and 3 with the right-angled and round bends, at different $Re_D$s. At $Re_D$ = 20,000, although the original MSC configurations with right-angled bends can provide better heat transfer enhancements, when N increases, $\eta$ decreases from 1.31 to 1.23 due to the high expense of total pressure loss. However, at $Re_D$ = 30,000 and 40,000, the trends are different: the values of thermal performance rise up with N. The reason is that, according to the definition of thermal performance, at the large $Re_D$s (30,000 and 40,000), the enhancement of $Nu/Nu_0$ obtained by increasing N exceeds the cost of $(f/f_0)^{1/3}$.

After the modification of right-angled bends to round bends, the friction loss decreases noticeably. As a result, MSC configurations can provide much higher thermal performances at all $Re_D$s, especially in the case of N = 3.

## 5. Conclusions

This paper presents a novel multistage swirl cooling (MSC) conception, aiming to improve the internal cooling performances of turbine blade leading edges. Different from the traditional single-stage swirl cooling, the vortex chamber of MSC contains two or three stages. A series of numerical simulations are conducted using conjugate heat transfer algorithm, a real blade model and under real turbine operation conditions. Through the comparisons of heat transfer, fluid flow and thermal performances between different swirl cooling configurations, the following important conclusions can be drawn:

- The Nusselt number on the vortex chamber wall increases with the stage number. In the three-stage swirl cooling configuration, the averaged Nusselt number is 75% higher than that of the single-stage structure at least, and the Nusselt number distribution is also more uniform than that of the single-stage configurations.
- The overall cooling effectiveness on the leading edge surface increases with coolant Reynolds number, and the benefits of MSC are more obvious at high Reynolds numbers. At $Re_D$ = 40,000, the surface temperature averaged over the entire leading edge wall of the three-stage swirl cooling model is close to 100 K lower than that in the single-stage configuration.
- The coolant allocation to different nozzles in MSC configuration is more uniform compared to the traditional single-stage model. For all the three swirl cooling configurations, large-scale spiral vortex structures can be observed in the vortex chambers, but the tangential velocities of coolant exiting from the nozzles are significantly higher in MSC structures.
- The heat transfer enhancement of MSC configuration is at the cost of the higher total pressure loss, which mainly happens in the bend region. If the right-angled bend is modified into round bend, the pressure loss falls quickly.

- After the modification of the bend shape, at all $Re_D$s, the thermal performances of two MSC configurations are much higher than that of the single-stage swirl cooling configuration.

## Declaration of competing interest

The authors declare that they have no known competing financial interests or personal relationships that could have appeared to influence the work reported in this paper.

## Data availability

Data will be made available on request.

## Acknowledgements

The authors would like to thank for the financial support from Shenyang Aero-engine Institute of Aviation Industry Corporation of China and computational support from the Supercomputing Center in the University of Science and Technology of China.

## References

[1] J.C. Han, S. Dutta, S. Ekkad, Gas Turbine Heat Transfer and Cooling Technology, CRC Press, 2012.
[2] P. Ligrani, Heat transfer augmentation technologies for internal cooling of turbine components of gas turbine engines, Int. J. Rotating Mach. 3 (2013), 2013.
[3] F. Kreith, D. Margolis, Heat transfer and friction in turbulent vortex flow, Appl. Sci. Res. 8 (1959) 457–473.
[4] B. Glezer, T. Lin, H.K. Moon, An Improved Turbine Cooling System, U.S. Patent No, 1997, p. 5603606.
[5] B. Glezer, H.K. Moon, J. Kerrebrock, J. Bons, G. Guenette, Heat transfer in a rotating radial channel with swirling internal flow, in: ASME Turbo Expo vol. 98, 1998. GT-214.
[6] P.M. Ligrani, C.R. Hedlund, B.T. Babinchak, R. Thambu, H.-K. Moon, B. Glezer, Flow phenomena in swirl chambers, Exp. Fluid 24 (1998) 254–264.
[7] C.R. Hedlund, P.M. Ligrani, Local swirl chamber heat transfer and flow structure at different Reynolds numbers, J. Turbomach. 122 (2000) 375–385.
[8] P.M. Ligrani, M.M. Oliveira, T. Blaskovich, Comparison of heat transfer augmentation techniques, AIAA J. 41 (2003) 337–362.
[9] J.P.C.W. Ling, P.T. Ireland, N.W. Harvey, Measurement of heat transfer coefficient distributions and flow field in a model of a turbine blade cooling passage with tangential injection, ASME Turbo Expo (2006) GT2006–90352.
[10] Christoph Biegger, Corrado Sotgiu, Bernhard Weigand, Numerical investigation of flow and heat transfer in a swirl tube, Int. J. Therm. Sci. 96 (2015) 319–330.
[11] Y. Rao, C. Biegger, B. Weigand, Heat transfer and pressure loss in swirl tubes with one and multiple tangential jets pertinent to gas turbine internal cooling, Int. J. Heat Mass Tran. 106 (2017) 1356–1367.
[12] Z. Liu, J. Li, Z. Feng, T. Simon, Numerical study on the effect of jet nozzle aspect ratio and jet angle on swirl cooling in a model of a turbine blade leading edge cooling passage, Int. J. Heat Mass Tran. 90 (2015) 986–1000.
[13] Z. Liu, J. Li, Z. Feng, Numerical study of swirl cooling in a turbine blade leading edge model, J. Thermophys. Heat Tran. 29 (1) (2015) 166–178.
[14] C. Du, L. Li, X. Wu, Z. Feng, Effect of jet nozzle geometry on flow and heat transfer performance of vortex cooling for gas turbine blade leading edge, Appl. Therm. Eng. 93 (2016) 1020–1032.
[15] C. Du, L. Li, Z. Feng, Effects of aerodynamic parameters on steam vortex cooling behavior for gas turbine blade leading edge, Proc. Inst. Mech. Eng. (2016), 0957650916636974.
[16] C. Du, L. Li, X. Fan, Numerical study on vortex cooling flow and heat transfer behavior under rotating conditions, Int. J. Heat Mass Tran. 105 (2017) 638–647.
[17] X. Fan, L. Li, J. Zou, J. Wang, F. Wu, Local heat transfer of vortex cooling with multiple tangential nozzles in a gas turbine blade leading edge cooling passage, Int. J. Heat Mass Tran. 126 (2018) 377–389.
[18] X. Fan, L. Li, J. Zou, Y. Zhou, Cooling methods for gas turbine blade leading edge: comparative study on impingement cooling, vortex cooling and double vortex cooling, Int. Commun. Heat Mass Tran. 100 (2019) 133–145.
[19] K. Liu, Q. Zhang, A novel multi-stage impingement cooling scheme - Part I: concept study, J. Turbomach. 142 (2020) 1–31.
[20] K. Liu, Q. Zhang, A novel multi-stage impingement cooling scheme - Part 2: design optimization, J. Turbomach. 142 (2020) 1–31.
[21] X. Wang, H. Xu, J. Wang, W. Song, L. Wang, High pressure turbine blade internal cooling in a realistic rib roughened two-pass channel, Int. J. Heat Mass Tran. 170 (2021) 121019.
[22] T. Arts, Convective heat transfer with film cooling around a rotor blade, Modern Research Topics in Aerospace Propulsion (1991) 253–274.
[23] ANSYS Fluent Theory Guide 16.0, Fluent Inc., 2015.
[24] Z. Yu, C. Li, B. An, J. Liu, G. Xu, Experimental investigation of film cooling effectiveness on a gas turbine blade pressure surface with diffusion slot holes, Appl. Therm. Eng. 168 (2020) 114851.
[25] M. Kim, D.H. Shin, J.S. Kim, B.J. Lee, J. Lee, Experimental investigation of effusion and transpiration air cooling for single turbine blade, Appl. Therm. Eng. 182 (2021) 116156.
[26] J.P. Holman, Heat Transfer, Mc Gran-Hill Book Company, Soythern Methodist University, 1986.
[27] K.C. Mills, Y. Su, Z. Li, R.F. Brooks, Equations for the calculation of the thermophysical properties of stainless steel, ISIJ Int. 44 (10) (2004) 1661–1668.
[28] Florian R. Menter, Two-equation eddy-viscosity turbulence models for engineering applications, AIAA J. 32 (8) (1994) 1598–1605.
[29] E.N. Sieder, G.E. Tate, Heat transfer and pressure drop of liquids in tubes, Ind. Eng. Chem. 28 (1936) 1429–1436.
[30] B.S. Petukhov, Advances in Heat Transfer, vol. 6, Academic Pressure, New York, 1970.